



Investigating 3D microbial community dynamics of the rhizosphere using quantitative phase and fluorescence microscopy

Oumeng Zhang^{a,1}, Reinaldo E. Alcalde^{b,1}, Haowen Zhou^a, Siyuan Yin^a, Dianne K. Newman^{b,c}, and Changhuei Yang^{a,2}

Affiliations are included on p. 9.

Edited by Hui Cao, Yale University, New Haven, CT; received February 16, 2024; accepted July 1, 2024

Microbial interactions in the rhizosphere contribute to soil health, making understanding these interactions crucial for sustainable agriculture and ecosystem management. Yet it is difficult to understand what we cannot see; among the limitations in rhizosphere imaging are challenges associated with rapidly and noninvasively imaging microbial cells over field depths relevant to plant roots. Here, we present a bimodal imaging technique called complex-field and fluorescence microscopy using the aperture scanning technique (CFAST) that addresses these limitations. CFAST integrates quantitative phase imaging using synthetic aperture imaging based on Kramers-Kronig relations, along with three-dimensional (3D) fluorescence imaging using an engineered point spread function. We showcase CFAST's practicality and versatility in two ways. First, by harnessing its depth of field of more than 100 µm, we significantly reduce the number of captures required for 3D imaging of plant roots and bacteria in the rhizoplane. This minimizes potential photobleaching and phototoxicity issues. Second, by leveraging CFAST's phase sensitivity and fluorescence specificity, we track microbial growth, competition, and gene expression at early stages of colony biofilm development. Specifically, we resolve bacterial growth dynamics of mixed populations without the need for genetically labeling environmental isolates. Moreover, we find that gene expression related to phosphorus sensing and antibiotic production varies spatiotemporally within microbial populations that are surface attached and appears distinct from their expression in planktonic cultures. Together, CFAST's attributes overcome commercial imaging platform limitations and enable insights to be gained into microbial behavioral dynamics in experimental systems of relevance to the rhizosphere.

fluorescence imaging | quantitative phase imaging | rhizosphere | colony biofilms | microbial communities

The nuanced biological processes within the rhizosphere (the zone of the soil in the vicinity of plant roots) play a crucial role in nutrient cycling, plant health, soil carbon dynamics, water quality, and microbial ecology (1-7). Advanced imaging methods, including confocal microscopy and molecular imaging techniques, enable real-time visualization, spatial mapping, and quantitative analysis of microbial activities around plant roots in a lab environment. They have the potential to track changes over time, aiding in the identification of microbial populations, biofilm structures, and nutrient gradients (8-13). Additionally, they can provide molecular and functional insights, such as real-time bacterial gene expression within the rhizosphere microbiota, but such applications are few and far between (14) due to complex geometry and dynamic interactions between roots and bacteria that are difficult to image.

For example, fluorescence imaging offers exceptional specificity for differentiating components within the rhizosphere, yet to capture their full three-dimensional (3D) dynamics, traditional fluorescence microscopy often necessitates axial scanning. This approach slows down the imaging process and increases the risks of photobleaching and phototoxicity. Recently, the ability to resolve the 3D fluorescence distribution without scanning the sample has been made possible through advances in point spread function (PSF) engineering (15–17) combined with computational methods (18–20). These methods involve the modulation of light at the pupil of a microscope, thereby altering the detected image to encode 3D information within a two-dimensional (2D) image. Another challenge in fluorescence imaging is that labeling is not always a viable option for environmental samples. Hence, a noninvasive imaging approach would be particularly valuable for imaging the rhizosphere. Quantitative phase imaging (QPI) methods, such as quantitative differential phase contrast (21, 22), digital holography (23–25), and Fourier

Significance

The rhizosphere—the soil region influenced by plant roots—is home to a multitude of microbes. Despite their importance to agriculture and diverse ecosystems, these biological communities are poorly understood in part due to limited real-time imaging capability. Here, we introduce complex-field and fluorescence microscopy using the aperture scanning technique (CFAST), an innovative imaging system merging three-dimensional (3D) fluorescence with quantitative phase imaging. CFAST's exceptional depth of field enables efficient 3D volume scanning, reducing bleaching risks associated with traditional fluorescence imaging. Its noninvasive approach facilitates observing interactions and gene expression within and among bacterial taxa, even those not yet genetically tractable. Overall, CFAST holds promise as a valuable tool for studying complex biological community dynamics in the rhizosphere.

Author contributions: O.Z., R.E.A., D.K.N., and C.Y. designed research; O.Z., R.E.A., and S.Y. performed research; O.Z., R.E.A., and H.Z. analyzed data; and O.Z., R.E.A., D.K.N., and C.Y. wrote the paper.

The authors declare no competing interest.

This article is a PNAS Direct Submission.

Copyright © 2024 the Author(s). Published by PNAS. This article is distributed under Creative Commons Attribution-NonCommercial-NoDerivatives License 4.0 (CC BY-NC-ND).

¹O.Z. and R.E.A. contributed equally to this work.

²To whom correspondence may be addressed. Email: chyang@caltech.edu.

This article contains supporting information online at https://www.pnas.org/lookup/suppl/doi:10.1073/pnas. 2403122121/-/DCSupplemental.

Published August 6, 2024.

ptychographic microscopy (26-28), emerge as less explored yet promising options in this context. These techniques capture the complex optical field as light passes through the sample. Despite their lower specificity compared to fluorescence imaging, they offer distinct advantages such as high sensitivity when visualizing low-contrast samples. Several bimodal imaging systems that combine QPI with fluorescence imaging have been developed during the past decade (29–37). Unlike earlier approaches that directly added QPI paths to existing epifluorescence microscopes (29–31), some recent approaches integrate QPI and fluorescence imaging more effectively, minimizing the overall number of components required (33–35, 37). However, a remaining challenge is that the optical components used in QPI, such as those used in off-axis holographic setups, typically do not overlap with those that are optimal for fluorescence imaging, and vice versa. Therefore, efficiently achieving both QPI and fluorescence imaging within a single system remains a challenging task.

$$S_{i}(u,v) = \mathcal{F}\left\{\exp\left(\frac{\ln\left(I_{i}(x,y)\right)}{2} + j\mathcal{F}^{-1}\left\{\mathcal{F}\left\{\frac{\ln\left(I_{i}(x,y)\right)}{2}\right\} \cdot H_{i}(u,v)\right\}\right)\right\},\tag{1}$$

Recently, the synthetic aperture imaging based on Kramers-Kronig relations (KKSAI) (38) that adopts simple pupil manipulation has been proposed for QPI. It conceptually resembles Schlieren imaging techniques (39, 40), which capture the phase gradient of light passing through transparent media. In Schlieren imaging, a spatial filter in the Fourier plane, e.g., a Foucault knife-edge, acts as a Hilbert transform (41–43) and enables quantitative measurements. Although both methods share the simplicity of their optical setups, KKSAI extends beyond imaging pure phase objects to capturing both the amplitude and phase of any object. Additionally, unlike other QPI techniques that use complex pupil modulation, such as spiral phase contrast microscopy (44), KKSAI uses binary amplitude modulation directly on the pupil and is not sensitive to wavelength changes. This feature makes it ideal for simultaneously modulating both illumination and fluorescence, rendering it compatible with PSF engineering and thus allowing it to offer complementary information when imaging microbial communities associated with plant roots.

In this study, we present complex-field and fluorescence microscopy using the aperture scanning technique (CFAST), a bimodal imaging approach designed to overcome the aforementioned limitations to better study plant-microbe and microbe-microbe interactions in a lab setting. CFAST represents a bimodal approach merging 3D fluorescence and complex field (quantitative phase) imaging using KKSAI, delivering uniform resolution over an extended depth of field. Here, we demonstrate the capability of CFAST to provide detailed, noninvasive images of rhizosphere organisms across different length scales. While these experiments represent our initial steps toward imaging the rhizosphere in situ, more generally, CFAST holds promise as an instrument through which to gain insight into biological dynamics in complex environments.

Results

System Schematic and Operating Principle. The schematic of CFAST is illustrated in Fig. 1A. A 4f system (L1 and L2) was integrated into a conventional wide-field microscope to modulate light at the pupil of the objective lens. The system uses a plane wave from a laser to illuminate the sample and excite the fluorophores simultaneously. A spinning disk (SD) aperture, the heart of this design, is positioned at the back focal plane (BFP) of the 4f system,

blocking three-quarters of the pupil. The spinning disk stops at four specific orientations [Fig. 1A (1-4)] during the acquisition of fluorescence and brightfield images. A dichroic mirror (DM) subsequently separates the fluorescence and illumination light, which are then captured by two cameras.

KKSAI (38) was utilized for QPI. The aperture is aligned such that the normal incidence (NI) component of the illumination laser passes through its corner (Fig. 1B). This unscattered NI component and the portion of the scattered light fields that transmit through the aperture interfere with each other at the image plane, and the resulting image is detected by one of the cameras. Briefly, the Kramers-Kronig (KK) relations establish bidirectional connections between the real and imaginary components of a complex function that is analytic in the upper half-plane (45, 46). In KKSAI, the (shifted) complex optical field S_i of the opening of the spinning disk, termed subaperture, corresponding to each detected image $I_i (i \in \{1, 2, 3, 4\})$ can be written as (38)

where (u, v) and (x, y) are the coordinates at the pupil and image planes, \mathcal{F} is the Fourier transform, and $H_i(u, v)$ represents a Hilbert kernel that depends on the subaperture position (see Materials and Methods for more details). After shifting and stitching the fields of four subapertures, the phase and amplitude of the sample are obtained from the complete optical field of the pupil through a Fourier transform.

We experimentally demonstrated KKSAI by imaging 5-µm radius fluorescent beads on a tilted cover glass (Fig. 1D). Four brightfield images (I_i , Fig. 1 D, i) were captured to compute S_i according to Eq. 1. Although the recovered complex optical field (amplitude and phase, Fig. 1 D, ii) is 2D, it enables us to digitally generate a z-stack (SI Appendix, Fig. S1) by introducing a defocusing phase to the pupil (47, 48). For example, the sharpest focus of the top, middle, and bottom beads within the boxed sections in Fig. 1 D, ii corresponds to axial positions of -26, -3, and 22 µm, respectively. This indicates an approximate cover glass tilt of 15°.

The principle of 3D fluorescence imaging resembles the multiview reflector microscope (49) and the Fourier light-field microscope (50). Given that only part of the pupil gets imaged in each of the four frames, the images corresponding to a point source exhibit apparent lateral shifts as the source defocuses (SI Appendix, Fig. S2); each frame has a unique shift direction. The theoretical and experimental PSFs are shown in Fig. 1C. The 3D fluorescence imaging procedure is shown in Fig. 1E; four fluorescence images of the aforementioned fluorescent beads (Fig. 1 E, i) were analyzed using a modified Richardson-Lucy deconvolution algorithm (50-53) (Materials and Methods). The reconstructed 3D images (Fig. 1 E, ii and iii) confirm the cover glass tilt, consistent with the KKSAI results (Fig. 1D). The deconvolution algorithm was also validated using synthetic data (SI Appendix, Fig. S3), indicating CFAST outperforms other widely used 3D PSFs (15, 54).

To quantify the resolution of 3D fluorescence imaging in CFAST, we imaged 100-nm fluorescent beads at various axial positions and measured the full width at half maximum (FWHM) of the xy and xz cross-sections of the reconstruction (Fig. 1F). The experimental resolution along the lateral and axial directions are 0.6 ± 0.1 and 1.9 ± 0.1 µm for in-focus beads, respectively (Fig. 1G). The lateral resolution is consistent with the theoretical diffraction limit and remains consistent within a 20-µm depth of

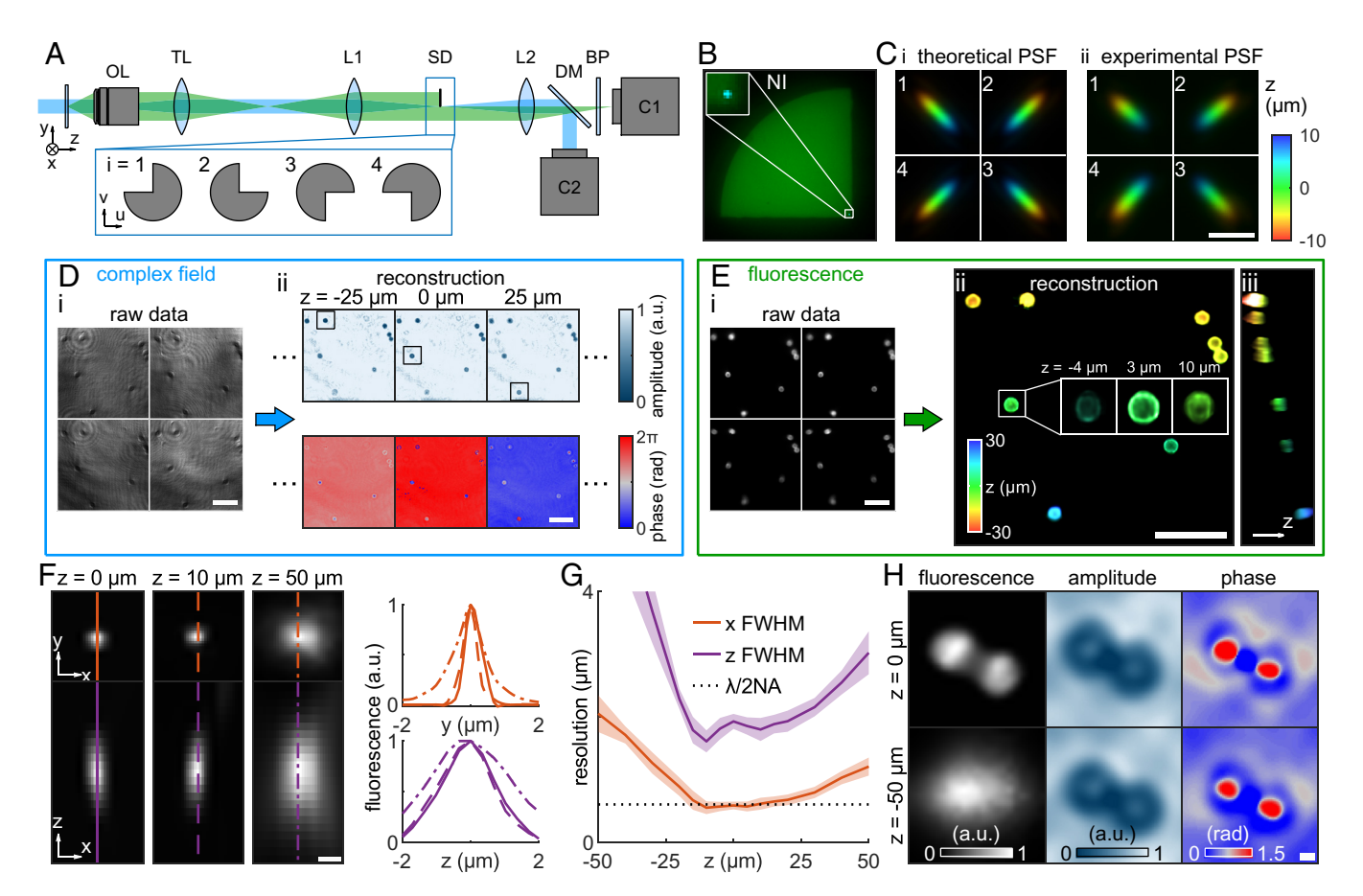


Fig. 1. Schematic and working principle of CFAST. (A) OL, objective lens; TL, tube lens; L1 and L2, 4f lenses; SD, spinning disk; DM, dichroic mirror; BP, bandpass filter. Four brightfield images and four fluorescence images are captured by detectors C1 and C2, respectively, at different orientations of SD ($i \in \{1, 2, 3, 4\}$). Blue represents the illumination laser; green represents the fluorescence. (B) Image of the back focal plane when SD is oriented as depicted in (A) (i = 1). The illumination laser is aligned such that the normal incident (NI) component is at the corner of the SD. (C) (i) Theoretical and (ii) experimental PSFs within a depth of field of 20 µm. (D) Workflow of phase imaging. (i) Four raw images of 5-µm (radius) fluorescent beads on a tilted cover glass are analyzed using the complex field reconstruction algorithm, generating a z stack of the amplitude and phase images. (E) Workflow of fluorescence imaging. (i) Four raw images of the aforementioned sample are analyzed using a 3D deconvolution algorithm (Materials and Methods), generating (ii and iii) fluorescence images of the whole 3D volume. (ii) The xy view; (iii) the yz view. (F) The xy and xz cross-section and the corresponding line profiles of the 3D fluorescence reconstruction of a 100-nm bead at different axial positions. (G) The (orange) lateral and (purple) axial resolution of the fluorescence imaging in CFAST is determined using the FWHM of the line profiles. Lines and shaded areas represent the average and SD across 63 beads. (H) Fluorescence, amplitude, and phase reconstruction of two 1.25-µm beads that are (Top) in focus and (Bottom) defocused by 50 μm. Scale bar, 5 μm in (C); 50 μm in (D and E); 1 μm in (F and H).

field. The axial resolution shows a slight enhancement with a defocus of ±10 µm. Notably, this depth of field significantly outperforms the specification of the objective lens (depth of field = 1.6 μm, 20×, 0.42 NA). This improved depth of field is attributed to the smaller effective NA of the CFAST imaging system; our measurements indicate an effective NA that is approximately 40% of the objective lens's NA (SI Appendix, Supplementary Note S1). Further, compared to the 20-µm depth of field of 3D fluorescence imaging, KKSAI shows a more extensive depth of field (SI Appendix, Fig. S4). The enhancement arises because, unlike in fluorescence imaging where the depth of field is limited by the effective NA, the limits of digital refocusing in coherent imaging are primarily determined by the spatial and temporal coherence of the illumination source and the accuracy of the reconstructed complex field (55). Previous studies have shown that QPI with LED illumination can typically extend the depth of field by a factor of 3 to 6 (26, 56, 57), while laser illumination can achieve an improvement up to a factor of 40 (58). For instance, when two 1.25-µm fluorescent beads are ~3 µm apart, the 3D fluorescence algorithm fails to recover both spheres when defocused by $50~\mu m$, whereas complex field images still resolve the separation (Fig. 1H).

The bimodal imaging provided by CFAST offers numerous advantages. In the following sections, we show applications with

plant roots and bacteria to highlight that 1) the long depth of field of QPI (more than 100 µm, SI Appendix, Fig. S5) optimizes the number of slices required for axial scanning, improving the efficiency of 3D fluorescence imaging, and 2) QPI provides an additional dimension that complements fluorescence imaging (e.g., SI Appendix, Fig. S6).

Bimodal Imaging of Plant Roots and Bacteria on the Rhizoplane with Varying Depth of Field. Standard scanning techniques, such as confocal imaging, are typically slow when capturing 3D volumes. Moreover, given the intricate nature of plant roots, their thickness often varies considerably across different sections. Therefore, scanning a target region without a prior understanding of its thickness can result in suboptimal scan speeds and risk overexposing the specimen to excitation light, potentially accelerating photobleaching and phototoxicity. CFAST offers a solution to this limitation by leveraging the long depth of field of KKSAI; the thickness of the sample can be determined by obtaining amplitude and phase images at just one axial position.

We demonstrated this ability of CFAST by imaging the 3D morphology of maize roots through its autofluorescence (Fig. 2 A and B and SI Appendix, Figs. S7 and S8A). In a thin section of the maize root, the recovered amplitude (Fig. 2 A, i) shows both edges

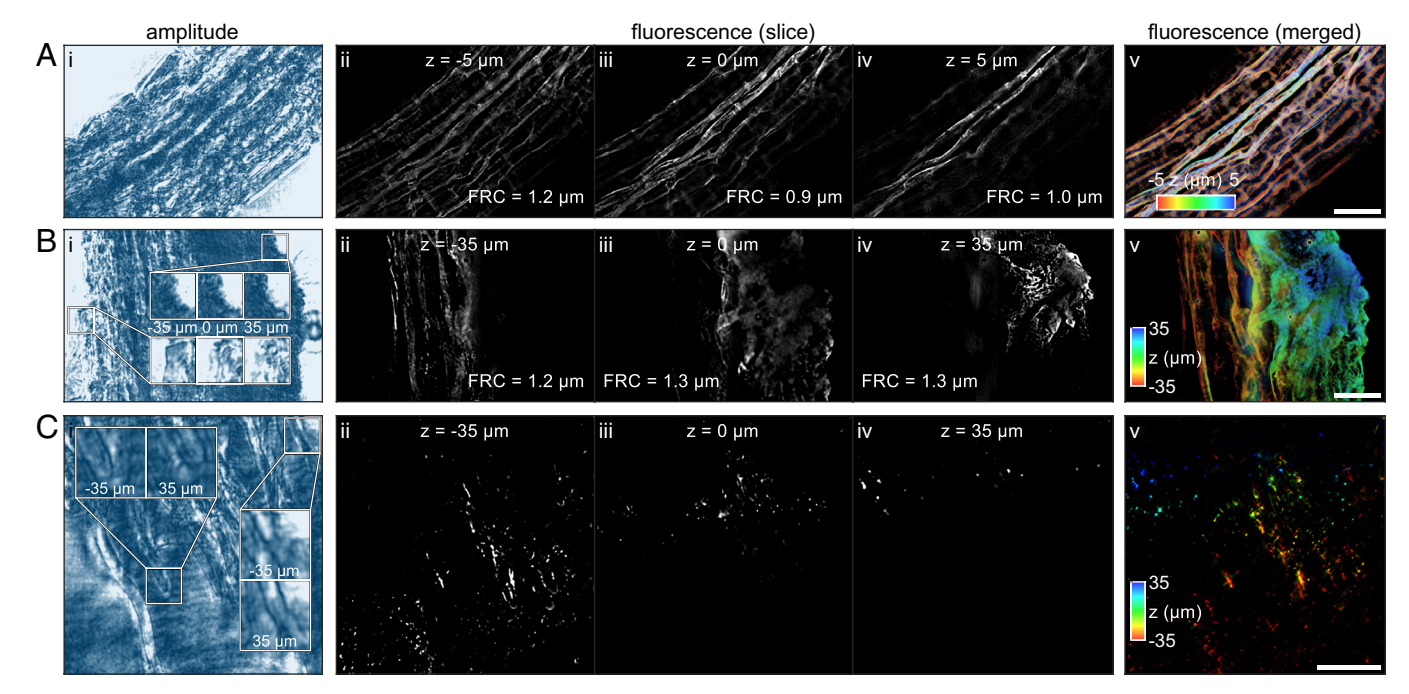


Fig. 2. CFAST 3D imaging of maize roots. (*A*) A thin section and (*B*) a thick section on the root. (*C*) Imaging of fluorescent bacteria on thick sections of roots. (*i*) Amplitude images, (*ii–iv*) reconstructed fluorescence images at various axial slices, and (*v*) 3D fluorescence images. Color bar, axial position. (Scale bar, 50 μm.)

with sharp focus simultaneously, eliminating the need of additional axial positions to capture the full 3D fluorescence distribution (Fig. 2 *A*, *ii*–*v*). In contrast, for a thick region of the same root, KKSAI indicates a 70-µm axial difference between its left and right sections (Fig. 2 *B*, *i* and *SI Appendix*, Figs. S9–S11 *A* and *B*).

Considering the depth of field of 20 μm in 3D fluorescence imaging, we deduced that capturing at least four axial positions is essential for the full 3D volume reconstruction (Fig. 2 B, ii–v). Fourier ring correlation (59) analysis shows lateral resolutions of 0.9 to 1.2 μm in the thin sections and 1.2 to 1.3 μm in the thick sections.

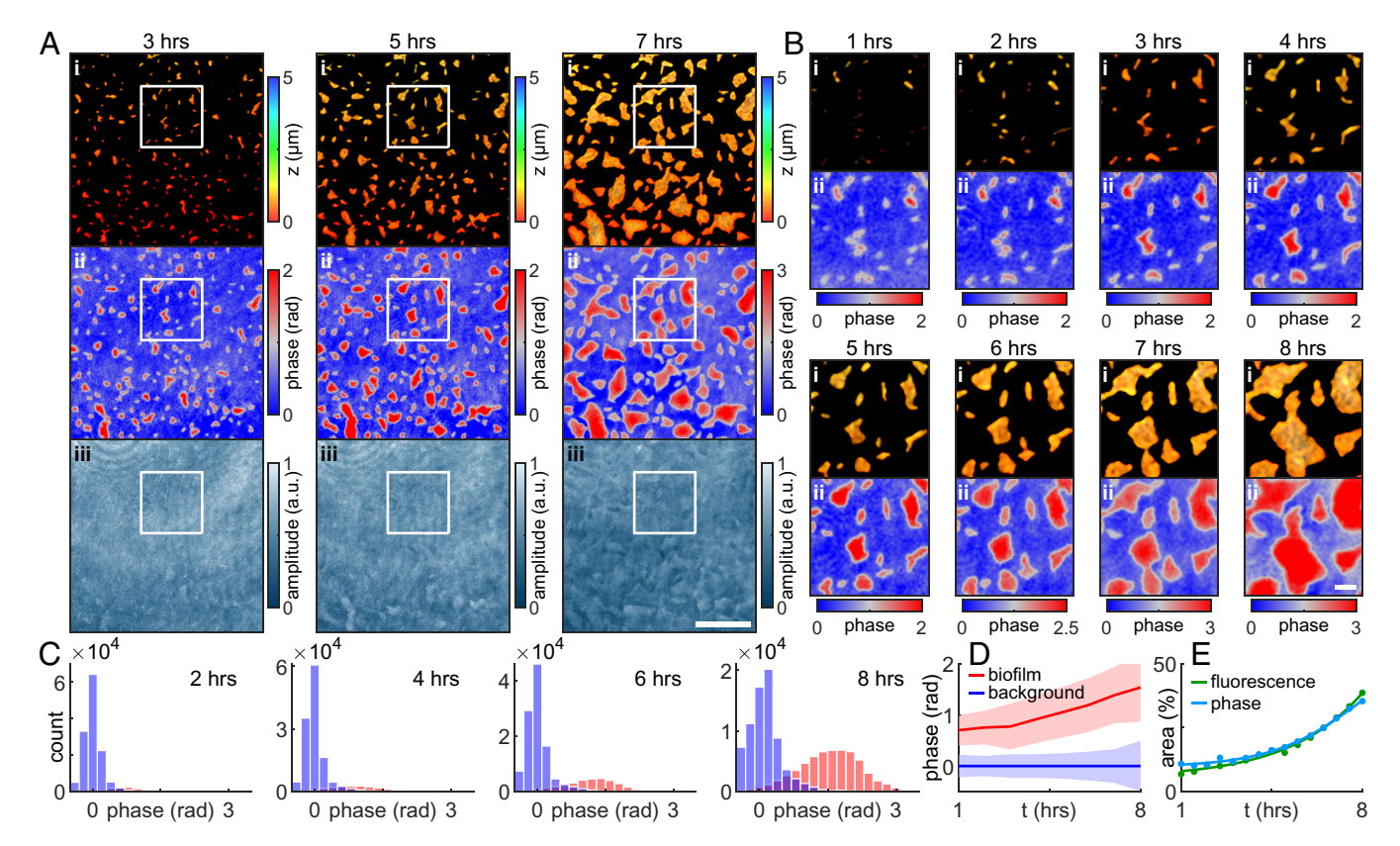


Fig. 3. Time-lapse CFAST imaging of bacterial biofilm formation. (*A*) Images of *P. synxantha* P_{PA10403}-mNeonGreen (*P. syn-mNG*) growing on MOPS-based defined agar medium. (*B*) The boxed region in (*A*). (*i*) Fluorescence images, (*ii*) quantitative phase images, (*iii*) amplitude images. Color bar, axial position in (*i*); phase in (*ii*); amplitude in (*iii*). Scale bar, 50 µm in (*A*); 10 µm in (*B*). (*C*) Distribution of phase values in the (red) bacterial biofilm and (blue) background areas. (*D*) Phase values of both areas over time. An offset was subtracted such that the average phase within the background area is zero. Solid lines represent the average; shaded areas represent the SD. (*E*) Surface area of biofilm colony determined by the (light blue) quantitative phase images and (green) fluorescence images over time.

We then test the ability of our system to capture bacteria on the surface of roots (i.e., the rhizoplane) with minimal acquisitions (Fig. 2C and SI Appendix, Figs. S8B and S12). Here, we used a model host plant called Brachypodium distachyon (60) and a model rhizobacterium called Pseudomonas synxantha 2-79 (60, 61). We tagged P. synxantha with a constitutive reporter fluorophore (i.e., P. synxantha P_{PA10403}-mNeonGreen, P. syn-mNG) to track its presence on the rhizoplane of B. distachyon; previously similar Pseudomonas species have been used to visualize root-microbe interactions with B. distachyon (62). The thickness of the sample was obtained with amplitude and phase images at one axial point allowing us to deduce the number of captures required for visualizing the full volume of bacteria on the root surface. Considering a depth of field of 20 µm in 3D fluorescence imaging, we determined that four axial positions are required to obtain the 3D volume reconstruction of fluorescent bacteria on the root surface (Fig. 2 C, ii-v). Comparative experiments with confocal imaging (SI Appendix, Figs. S13 and S14) and negative control tests (SI Appendix, Fig. S15) further validate our observations.

Bimodal Imaging of Early-Stage Bacterial Colony Biofilm Formation.

Roots typically contain surface-associated microbes called biofilms (63). As a proof of principle for studying biofilm development, we demonstrated the utility of CFAST by imaging static bacterial aggregate development using a simple method to grow biofilms independent of

roots (64). Here, we tracked bacterial growth, competition, and gene expression during the early stages (i.e., within the first 24 h of growth) of biofilm formation.

We first conducted time-lapse imaging of P. syn-mNG on a MOPS-based defined agar medium (Fig. 3 A and B). The bacterial surface area (i.e., radial growth in 2D) was captured by the fluorescence images (Fig. 3 A and B, i). The amplitude images (Fig. 3 A, iii) show no morphological correlation with the fluorescence images (Fig. 3 A, i), suggesting that the growth cannot be observed using a conventional brightfield microscope. In contrast, quantitative phase images (Fig. 3 A and B, ii) closely mirror the fluorescence images (Fig. 3 \tilde{A} and \tilde{B} , i). The phase values within the biofilm area are easily distinguishable from the background (Fig. 3 C and D); the surface areas determined by the fluorescence and quantitative phase images exhibit a difference of less than 1.4% (Fig. 3E). This experiment establishes that QPI can be used to study early biofilm development.

We next examined the ability of our method to investigate competition between P. syn-mNG and two wheat isolates that are not yet genetically tractable. Here, areas with fluorescence signal pinpoint the location of *P. syn-mNG*, while those with large phase values but no fluorescence identify the nonfluorescent strains (SI Appendix, Fig. S16). We conducted a competition experiment with P. syn-mNG and Paraburkholderia graminis (P. gram), a recently collected wheat isolate (65). The initial concentration

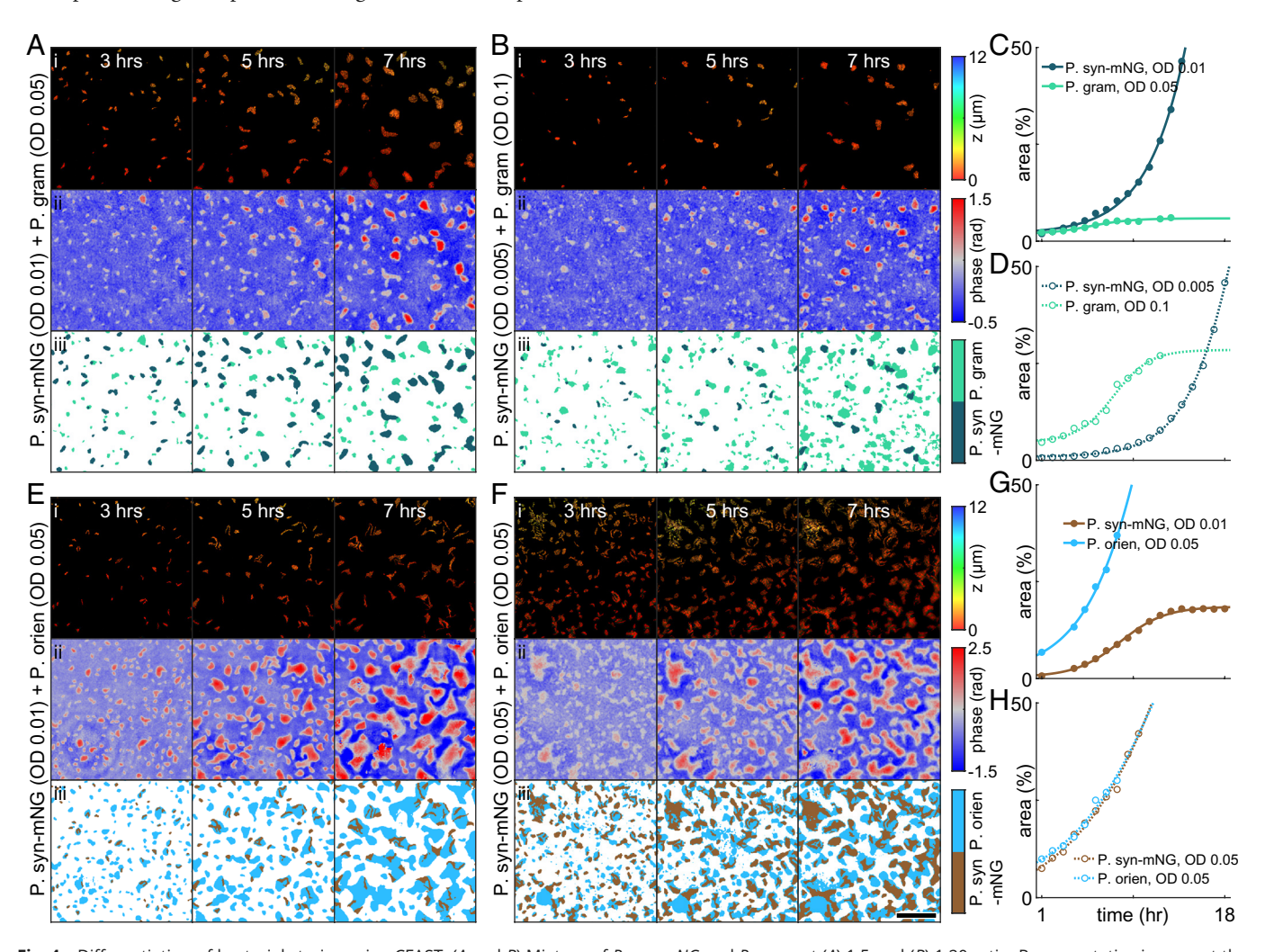


Fig. 4. Differentiation of bacterial strains using CFAST. (A and B) Mixture of P. syn-mNG and P. gram at (A) 1:5 and (B) 1:20 ratio. Representative images at the 3, 5, and 7-h timepoints showing that (i) fluorescence and (ii) quantitative phase images can be used to pinpoint (iii) different strains. (Scale bar, 50 µm.) Color bar, axial position in (i); phase in (ii). (C and D) Corresponding surface area percentage of different bacteria over time indicative of growth. (E-H) Mixture of P. syn-mNG and P. orien at (E and G) 1:5 and (F and H) 1:1 ratio.

ratios tested were 1:5 and 1:20 (*P. syn-mNG*: *P. gram*) (Fig. 4 *A* and *B*). At the 1:5 ratio, *P. gram* is immediately outgrown by *P. syn-mNG* (Fig. 4*C*); it reaches stationary phase at ~12 h, occupying 5.9% of the total area. With the 1:20 ratio, *P. gram* reaches stationary phase at ~13 h, ultimately covering 16.0% of the total area (Fig. 4*D*) yet is still outcompeted by *P. syn-mNG*. We then conduct a second competition experiment with *Pseudomonas orientalis* (*P. orien*) another wheat isolate. The initial concentration ratios tested were 1:5 and 1:1 (*P. syn-mNG*: *P. orien*) (Fig. 4 *E* and *F*). In this scenario, *P. orien* outcompetes *P. syn-mNG* at the 1:5 ratio, and no competition is observed between the strains at a 1:1 ratio (Fig. 4 *G* and *H*).

The 3D imaging capability of CFAST allows us to quantify spatiotemporal vertical growth dynamics during colony biofilm formation (Fig. 5). Aggregate 3D growth kinetics were visualized over time along with the merging of aggregates into microcolonies (Fig. 5 A and B). We obtained the thickness probability at specific time points (Fig. 5C) and a temporal progression of the thickness of all the aggregates and microcolonies within the field of view (Fig. 5D). This result indicates that the thickness of the P. syn-mNG aggregates is greater when grown in the presence of P. gram rather than P. orien, potentially due to less competition and more nutrient availability. Moreover, the morphologies (Fig. 5 A and B, i) of

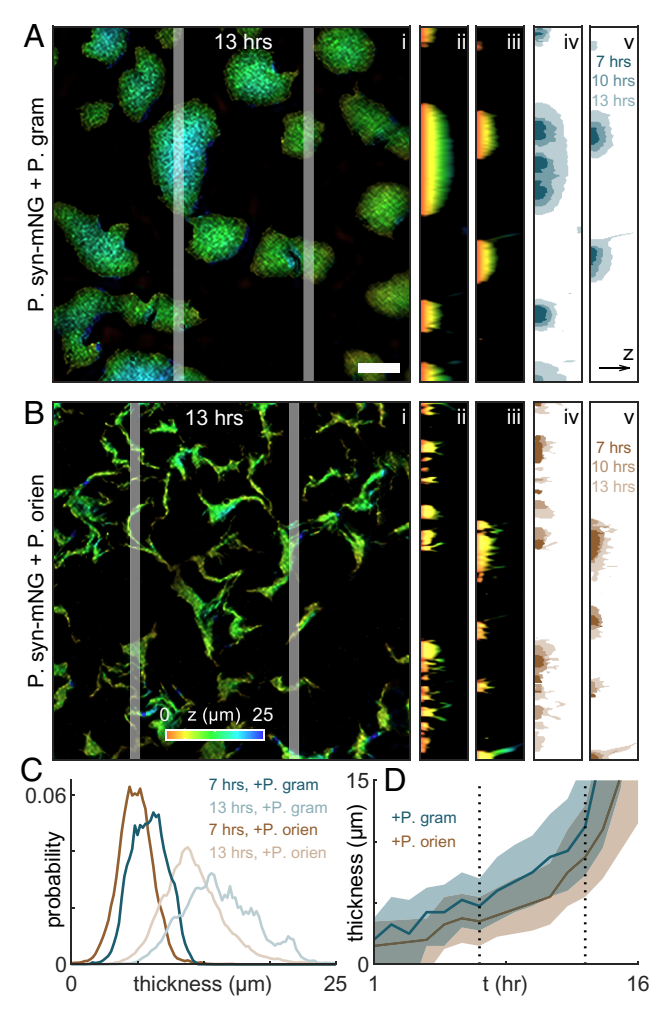


Fig. 5. CFAST imaging of 3D growth dynamics during colony biofilm formation. (A) Mixture of *P. syn-mNG* with *P. gram*, (B) mixture of *P. syn-mNG* and *P. orien*. (i) The xy-view, (ii and iii) the yz-view, and (iv and v) the corresponding timelapse vertical growth (yz-view). (Scale bar: 20 µm.) Color bar: height in microns. (C) Thickness distribution of *P. syn-mNG* colony biofilm at 7 h and 13 h. (D) Thickness distribution over time. Solid lines represent the median; shaded areas represent the 33rd and 67th percentile.

the *P. syn-mNG* aggregates with each competitor are strikingly different due to limitations and availability of space on the surface of the agar pad. Note that the 3D feature is not available for the quantitative phase images; although it is possible to digitally propagate the reconstructed 2D complex field, these images do not contain volumetric information, unlike 3D fluorescence images; multiple 2D complex field images are usually required to obtain a 3D volumetric reconstruction (66). Therefore 3D images are not generated for nonfluorescent strains. However, it is worth mentioning that the thickness of colonies can potentially be determined using quantitative phase measurements (67) with additional calibration in future studies.

Finally, we simultaneously imaged bacterial growth with complex field and gene expression with fluorescence using CFAST. Here, we constructed transcriptional fusion reporters to monitor gene expression associated with promotors sensing phosphorus limitation (*P. synxantha* P_{phoA} -mNeonGreen, *P. syn* P_{phoA} -mNG) and controlling phenazine biosynthesis (*P. synxantha* P_{phzA}-mNeonGreen, P. syn P_{phzA}-mNG). In Escherichia coli, the alkaline phosphatase, phoA, is up-regulated under phosphorus limitation (68), and the phzA-G operon in P. synxantha has been reported to be up-regulated either by phosphorus limitation or at high-cell densities due to quorum sensing (69–72). We confirmed these regulatory patterns with our constructs in planktonic conditions (SI Appendix, Fig. S17). Surprisingly, these gene expression patterns do not always hold when bacteria are surface-attached. Fig. 6A depicts the growth of P. syn P_{phoA}-mNG and induction of PphoA under phosphorus limitation: induction occurs radially as the aggregate grows. The periphery of the aggregate has minimal induction, consistent with the idea that the periphery still has sufficient amounts of phosphate. Induction of PphoA only occurs under phosphorus limitation and correlates with batch conditions (Fig. 6 A, B, and D and SI Appendix, Fig. S17). However, induction of PphzA does not occur under phosphorus-limited conditions but only after the surface area of the agar is uniformly covered by cells, indicating that induction under these conditions is due to quorum sensing only (Fig. 6 C and E). This result contrasts that of planktonic conditions, where induction occurs in response either to phosphorus limitations or quorum sensing (SI Appendix, Fig. S17).

Discussion

CFAST is a bimodal imaging technique that combines the strengths of both phase and fluorescence imaging. A key innovation of CFAST is the utilization of the spinning disk aperture, making it easy to integrate into existing commercial microscopes. Compared to other bimodal imaging techniques, due to its spinning disk aperture, CFAST more efficiently combines two imaging modalities: quantitative phase and 3D volumetric fluorescence imaging. Our results demonstrate that CFAST achieves lateral and axial resolutions of 0.6 and 1.9 μm , respectively. CFAST is also able to capture 3D volumes of diverse root morphologies with varying thicknesses, bacteria on roots, and bacterial biofilm gene expression and interspecies competitive dynamics in 3D.

CFAST has a powerful depth of field, as evident in our examination of maize roots, where it enabled adaptive rather than exhaustive sample scanning to capture the 3D fluorescence distribution. This feature is critical when imaging samples of varying thicknesses because it minimizes potential photobleaching of fluorophores and phototoxicity to the sample, all while enhancing imaging speed (see *SI Appendix*, *Supplementary Note S2* for detailed analysis of the photodamage). Moreover, we used the same technique to image bacteria on the surface of roots with minimal acquisitions. For perspective, the 70-µm thick sample we captured with four

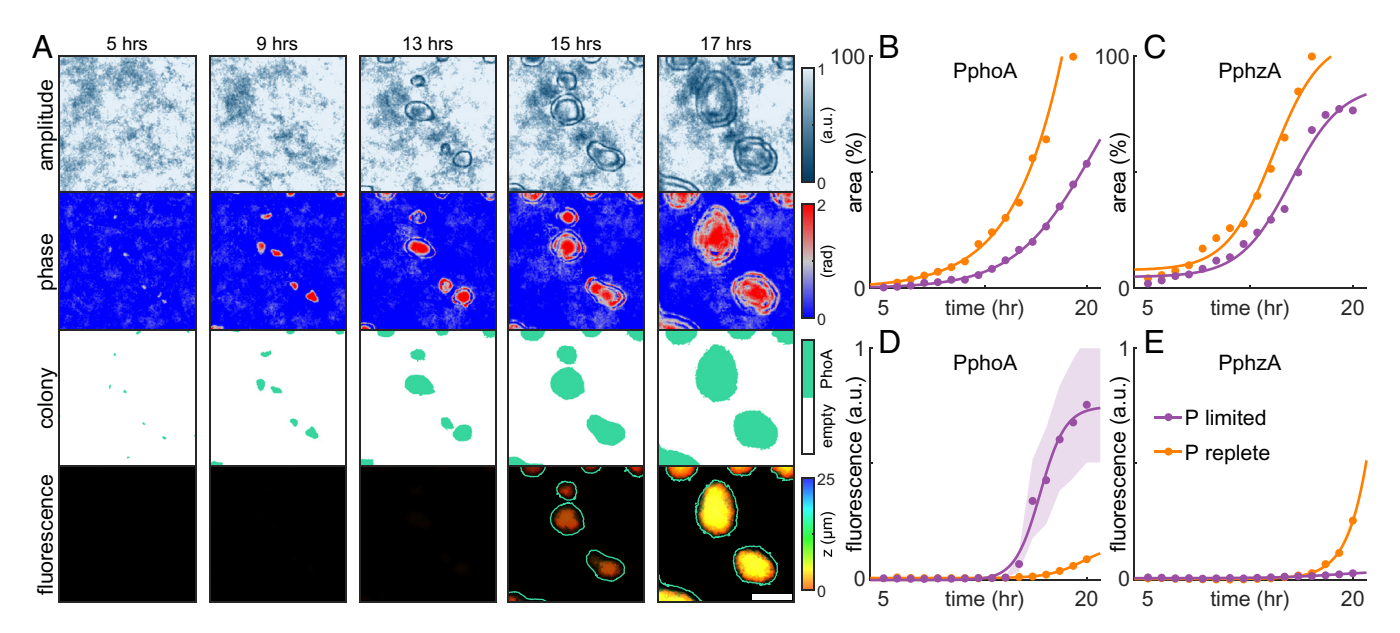


Fig. 6. CFAST imaging of gene expression. (*A*) Imaging of *P. syn* P_{phoA} -mNG under phosphorus (*P*) limitation. The growth is tracked by the complex field and gene expression by fluorescence. (Scale bar: 50 μ m.) (*B* and *C*) Surface area percentage indicative of growth and (*D* and *E*) fluorescence level of the (*B* and *D*) *P. syn* Pphod-mNG and (C and E) P. syn Pphzd-mNG colony biofilm over time. Shaded areas represent the 33rd and 67th percentile in (D and E). Purple: phosphorus-limited condition; orange: phosphorus-replete condition.

acquisitions at our axial resolution of 1.9 µm would require a minimum of 74 acquisitions with confocal microscopy when obtained with a 50% z-stacks overlap (optimal overlap). A 15% overlap would still require 44 image captures for similar resolution.

CFAST's phase sensitivity and fluorescence specificity is exemplified in our imaging of colony biofilm formation. The integration of quantitative phase and 3D fluorescence imaging enabled us to conduct spatiotemporal monitoring of early stages of biofilm growth and morphogenesis, visualize competitive growth of bacteria, identify vertical growth dynamics, and monitor gene expression spatiotemporally under varying environmental conditions. To date, most biofilm imaging methods capture aspects of these capabilities for bacteria harboring fluorescent proteins (73-78) but rarely do they focus on the early stages of biofilm development, much less for mixed microbial communities including nongenetically tractable bacteria. The 3D capacity offered by CFAST allows for autorefocusing on the desired focal plane using only four frames (SI Appendix, Figs. S11 C and D and S18), minimizing the risk of excessive laser exposure. Moreover, the ability to capture the 3D volume of 20-µm depth with a single capture minimizes photobleaching and phototoxicity. This is crucial for long-timescale imaging because we observe slower bacterial growth in laser-exposed regions (SI Appendix, Fig. S19). Finally, it is notable that induction of phenazine biosynthesis only occurs when aggregates and microcolonies have covered roughly 100% of the surface area with cells, and not in response to phosphorus limitation, unlike in planktonic culture. This unexpected result, consistent over several independent trials (SI Appendix, Fig. S20), raises the possibility that certain regulatory dynamics may be affected by surface-sensing and motivates future studies using CFAST to reveal unique phenomena in situ, paving the way for follow-up mechanistic research.

In conclusion, CFAST is a valuable tool for imaging complex biological systems. While achieving accurate volumetric refractive index imaging in the presence of strongly scattering and absorbing materials, such as soil particles, remains a challenge, CFAST performs well in clear or weakly scattering media. Looking ahead, we anticipate that CFAST will enable laboratory studies of how varying environmental conditions (be they from abiotic or biological sources) modulate microbial growth and gene expression on complex surfaces such as

roots. We plan to explore the potential for imaging bacterial growth on plant roots using quantitative phase, rather than fluorescence only, by employing multiple complex field images to reconstruct the full 3D refractive index distribution. This approach will allow us to determine the stages at which we can distinguish the phase signal of bacteria from the background roots. Furthermore, we aim to investigate the possibility of tracking the propagation of gene expression along the z-axis (i.e., through the thickness of a sample) in real time by taking advantage of CFAST's efficiency in reconstructing full 3D volumes from a minimal number of images during fluorescence imaging.

Materials and Methods

CFAST Imaging System. A 488-nm laser diode (Thorlabs LP488-SF20G) filtered by a laser line filter (Thorlabs FL488-3) is used to illuminate the sample. A 20 × , 0.42 NA long working distance objective lens (Mitutoyo Plan Apochromat) is used to capture the fluorescence and transmitted light. Two lenses (Fig. 1A, TL, Thorlabs AC254-100-A, L1, Thorlabs AC254-200-A) are used to project the pupil onto the spinning aperture (3D printed using CraftUnique Craftbot Plus, mounted on Thorlabs ELL14K). Another lens (Fig. 1A, L2, Thorlabs AC254-200-A) then projects the image plane onto the cameras (Imaging Source 33UX226). Typical exposure times are listed in SI Appendix, Table S1. A dichroic mirror (Thorlabs MD498) is used to separate the illumination light from fluorescence, and a bandpass filter (Thorlabs MF525-39) is used to further filter out residue illumination in the fluorescence path.

CFAST Forward Imaging Model. For QPI of an object s(x, y), the optical field at the pupil plane modulated by the spinning disk is given by

$$S_i(u, v) = \mathcal{F}\{s(x, y)\} \cdot P_i(u, v), i \in \{1, 2, 3, 4\},$$
 [2]

where \mathcal{F} represents the Fourier transform, (x, y) and (u, v) denotes the coordinates at sample and pupil planes, and $P_i(u, v)$ represents the binary amplitude mask defined by the ith spinning disk rotation angle. The camera then captures the intensity of the image plane, given by the square of the inverse Fourier transform of the modulated field $S_i(u, v)$,

$$I_{c,i}(x,y) = \left| \mathcal{F}^{-1} \left\{ S_i(u,v) \right\} \right|^2.$$
 [3]

For 3D fluorescence imaging, the images $\textbf{\textit{I}}_f = [I_{f,1}, I_{f,2}, I_{f,3}, I_{f,4}]$ are expressed as the convolution of an N-slice 3D object $\textbf{\textit{o}} = [o_{z_1}, o_{z_2}, \cdots, o_{z_N}]$ and the PSF of the

imaging system, i.e., $I_{f,i} = \sum_{k=1}^{N} o_{z_k} * \mathsf{PSF}_{i,z_k}$ where PSF_{i,z_k} represents the PSF for the i th image at axial position z_k . For simplicity, we define an operator \boldsymbol{H} that projects the object to the image space and rewrite the forward model as $\boldsymbol{I}_f = \boldsymbol{Ho}$.

CFAST Reconstruction Algorithm. To reconstruct the object s_i from four intensity measurements $I_{c,i}$, we first decompose the corresponding spectrum S_i into a scattered field S_i' and an unscattered plane wave,

$$I_{c,i}\big(x,y\big) = \left|\mathcal{F}^{-1}\big\{S_i'(u,v) + \delta(u,v)\big\}\right|^2 = \left|s_i'\big(x,y\big) + r\big(x,y\big)\right|^2, \quad \boldsymbol{[4]}$$

where $r(x,y)=e^{j\phi_0}$ represents the plane wave and ϕ_0 is a constant phase offset. Its Fourier transform is the Dirac delta function $\delta(u,v)$ corresponding to the NI component in Fig. 1*B*. To reconstruct the amplitude and phase of the optical field, we design an auxiliary function

$$X = ln\left(\frac{s_i'(x,y) + r(x,y)}{r(x,y)}\right),$$
 [5]

with a real part given by

$$\operatorname{Re}\{X\} = \frac{1}{2} \ln \left(\frac{I_{c,i}(x,y)}{\left| r(x,y) \right|^2} \right).$$
 [6]

It has been shown that X is analytical in the upper half-plane if the NI term is at the edge of the pupil and the unscattered light is stronger than the scattered light (38, 45, 46). Therefore, its imaginary part can be found using the Kramers-Kronig relation,

$$\operatorname{Im}\{X\} = \mathcal{F}^{-1}\left\{\mathcal{F}\left\{\operatorname{Re}\{X\}\right\} \cdot H_{i}(u,v)\right\},\tag{7}$$

where Hilbert kernel $H_i(u, v) = -j \operatorname{sgn} u \operatorname{for} i \in \{1, 2\}$ and $j \operatorname{sgn} u \operatorname{for} i \in \{3, 4\}$. Modulated fields S_i is therefore given by

$$S_i(u, v) = \mathcal{F}\left\{\exp\left(\operatorname{Re}\{X\} + j\operatorname{Im}\{X\}\right)r(x, y)\right\},$$
 [8]

yielding the expression in Eq. 1.

To reconstruct the 3D object \mathbf{o} from four detected fluorescence images \mathbf{I}_f , we implement a modified Richardson-Lucy method to iteratively find the solution. The deconvolution algorithm can be written as

$$\mathbf{o}^{(\rho+1)} = \frac{(\mathbf{H}^{\mathsf{T}}\mathbf{I})}{\left(\mathbf{H}^{\mathsf{T}}\mathbf{H}\mathbf{o}^{(\rho)}\right)} \odot \mathbf{o}^{(\rho)},$$
 [9]

where \odot represent the element-wise product. Operator \mathbf{H}^{T} performs the backward projection $\mathbf{H}^{\mathsf{T}}\widehat{\mathbf{I}} = \widehat{\boldsymbol{o}}$ where $\widehat{o}_{z_k} = \sum_{i=1}^4 \widehat{I}_i * \mathsf{PSF}'_{i,z_k}$. PSF'_{i,z_k} represents a 180°-rotated version of PSF_{i,z_k} .

Reconstruction algorithms were implemented in python and MATLAB R2023b. The deconvolution algorithm, implemented in python, processes a 600×600 -pixel FOV in 5.6 s on a NVIDIA 4090 GPU. The quantitative phase reconstruction and digital propagating to 100 axial planes, implemented in MATLAB, takes 2.2 s to execute on an AMD Ryzen9 $7900 \times$ CPU.

Maize and B. distachyon Root Preparation for Bimodal Imaging.

Maize preparation. Maize seeds were obtained from Home Depot (cat. Number 78031-6). Seeds were first sterilized with 70% ethanol for 20 s, rinsed with autoclaved water $3 \times$, placed in 50% bleach with 0.01% triton x for 3 min, and rinsed with autoclaved water $5 \times$. Seeds were then pregerminated on blot paper for 3 d. After germination, seedlings were transferred to 3 by 5-inch pots containing sterile sand. The maize plant was irrigated and watered with $0.5 \times$ Murashige and Skoog medium ($0.5 \times$ MS medium, Sigma-Aldrich, cat. Number M5524) adjusted to pH 5.8 with KOH. The plant was grown for roughly 3 mo at room temperature near a laboratory window. Roots were then collected and cleared with 1M KOH overnight and rinsed with 0.1M HCl before imaging.

B. distachyon preparation. B. distachyon BD21 seeds were first sterilized with chlorine gas following previous protocols. Seeds were then plated 0.6% phytagel (Sigma Aldrich, cat. Number P8169) containing 0.5 × MS medium (Sigma Aldrich cat Number M5519) and transferred to a growth chamber with a day/night cycle of 16 h/8 h at 25 °C for 2 d. After 2 d of growth, the seedlings were dipped for 30 min into 0.5 × MS medium containing bacteria at an OD600 of 0.1. Finally, they were gently transferred to the surface of a MatTek plate (MatTek, cat. Number P35G-1.5-20-C) containing 0.6% phytagel with 0.5 × MS medium and imaged shortly after.

Bacterial Strains and Medium Preparation.

Strains. Six bacterial strains were used in this study. They include wild-type *P. synxantha* 2-79 (gifted by Dmitri Mavrodi, University of Southern Mississippi, Hattiesburg, MS), *P. synxantha* P_{PA10403}-mNeonGreen (this study), *P. synxantha* P_{phoA}-mNeonGreen (this study), *P. synxantha* P_{phoA}-mNeonGreen (this study), *P. synxantha* P_{tac}-mCherry (gifted by Dmitri Mavrodi), *P. graminis* (wheat isolate), *P. orien* (wheat isolate). Wheat isolates were collected from a nonirrigated wheat field at Washington State University's Lind Dryland Research Station on August 9, 2019 (65)

Liquid medium. The strains were grown in a MOPS defined liquid medium (MOPS medium) containing: 4.1×10^{-4} M MgSO₄·7H₂O, 6.8×10^{-4} M CaCl₂·2H₂O, 1.6×10^{-2} M NH₄Cl, 7×10^{-3} M KH₂PO₄, 5.55×10^{-2} M glucose as the carbon source, $1 \times$ MEM amino acids solution (Gibco, 11130051), and a modified version of Aquil trace metals (79) containing 1×10^{-5} M Fe and 1×10^{-4} M EDTA. The medium was buffered with 25 mM MOPS to pH 7 (pH adjusted with 1 M NaOH). For 96-well plate experiments with limited phosphate, the concentration of KH₂PO₄ was reduced to 50×10^{-6} M KH2PO4.

Solid agar medium. Agar plates consisted of MOPS medium with 1% noble agar. For experiments with limited phosphate, the concentration of KH_2PO_4 in the agar plates was reduced to 10×10^{-6} M KH_2PO_4 . Two milliliters were pipetted into MatTek plates.

Fluorescent Reporter Construction. The transcriptional fusion fluorescent reporters were constructed using the mini-Tn7 vector insertion protocol from Choi and Schwiezer (80). A broad host-range mini-Tn7 vector was used for single-copy gene integration into the bacterial chromosomal at a neutral site located downstream of the highly conserved glmS site. We first cloned the desired inserts (i.e., promoters and mNeonGreen fluorophore) into the multiple cloning site of a pJM220 mini-Tn7 plasmid (Addgene, cat. Number 110559). Fragments were assembled using Gibson assembly (81) and electroporated into E. coli DH10B. Transformants were selected for on Luria-Bertani (LB) agar with gentamicin (20 μ g mL⁻¹). The presence of the correct construct was verified via PCR. Purified mini-Tn7 element DNA and pTNS1 helper plasmid (obtained from E. coli helper strains SM10/pTNS1) were then introduced into electrocompetent P. syn wild-type strain via electroporation. Transformants were selected for on LB agar with gentamicin (20 μg mL⁻¹). Correct constructs were confirmed by PCR, sanger DNA sequencing (Larage, Inc. Culver City, CA), and phenotype assays. See Planktonic 96-well plate assays for phenotype confirmation. A list of primers and plasmids used for each construct can be found in SI Appendix, Tables S2-S4.

Planktonic 96-Well Plate Assays. For all experiments, cells were initially inoculated from a -80 °C glycerol stock on LB broth overnight (16 to 18 h) at 30 °C shaking at 250 rpm. Cells were then washed 1× in MOPS medium that only contained 50 μM phosphate and plated onto a 96-well plate for an initial OD600 of 0.05. Each well contained 200 μL of media and 10 μL of inoculum. The plate reader (Tecan Spark 10M) was set to 30 °C with orbital shaking (Amplitude 2.5 mm, Frequency 216 rpm). Optical density (OD600) was collected at 600 nm and mNeonGreen fluorescence was collected at an excitation wavelength of 485 nm and emission wavelength of 585 nm. Data points were collected every 15 min for 24 h. Note that phosphorus-replete wells contained 7 mM phosphate and phosphorus-limited wells contained 50 μM phosphate.

Bimodal Colony Biofilm Imaging Experiments. For all experiments, cells were initially inoculated from a $-80\,^{\circ}\text{C}$ glycerol stock on MOPS defined liquid medium overnight (16 to 18 h) at 30 $^{\circ}\text{C}$ shaking at 250 rpm. Cells were then washed 1× in MOPS medium, diluted to an OD of 0.25, and grown for 4 to 5 h in MOPS medium. After this pregrowth, cells were washed 1× MOPS medium and diluted

to an OD of 0.05, unless otherwise stated in the main text. Cells were then spot plated on the MOPS agar medium by pipetting 5 μ L of sample to the center of the MatTek plate. Plates were air dried for 1 h with the lid off then transferred to the CFAST imaging platform containing a custom-made imaging chamber (SIAppendix, Fig. S21) used to limit water evaporation from the agar. Time-lapse images were collected every hour for 24 h. Note that for the phosphorus-limited experiments, the 5 μ L spotted cell sample contained 7 mM phosphate while the agar medium it was spotted onto only contained 10 µM phosphate.

Data, Materials, and Software Availability. Images and analysis code data have been deposited in OSF (https://osf.io/ak4wg/) (82).

- H. Toju et al., Core microbiomes for sustainable agroecosystems. Nat. Plants 4, 247–257 (2018).
- N. U. Mavrodi *et al.*, Recent insights into the diversity, frequency and ecological roles of phenazines in fluorescent Pseudomonas spp. *Environ. Microbiol.* **15**, 675–686 (2013).

 Y. Ma, R. S. Oliveira, H. Freitas, C. Zhang, Biochemical and molecular mechanisms of plant-microbemetal interactions: Relevance for phytoremediation. *Front. Plant Sci.* **7**, 918 (2016).

 S. B. Sharma, R. Z. Sayyed, M. H. Trivedi, T. A. Gobi, Phosphate solubilizing microbes: Sustainable
- approach for managing phosphorus deficiency in agricultural soils. Springerplus 2, 587 (2013).
- T. W. Crowther et al., The global soil community and its influence on biogeochemistry. Science 365, eaav0550 (2019).
- D. Naylor, D. Coleman-Derr, Drought stress and root-associated bacterial communities. Front. Plant Sci. 8, 2223 (2018).
- P. Prashar, N. Kapoor, S. Sachdeva, Rhizosphere: Its structure, bacterial diversity and significance. Rev. Environ. Sci. Biotechnol. 13, 63-77 (2014).
- H. Downie *et al.*, Transparent soil for imaging the rhizosphere. *PLoS One* **7**, e44276 (2012). H. Massalha, E. Korenblum, S. Malitsky, O. H. Shapiro, A. Aharoni, Live imaging of root-bacteria interactions in a microfluidics setup. Proc. Natl. Acad. Sci. U.S.A. 114, 4549-4554 (2017).
- M.-F. Noirot-Gros *et al.*, Functional imaging of microbial interactions with tree roots using a microfluidics setup. *Front. Plant Sci.* **11**, 408 (2020).
- M. Maisch, U. Lueder, A. Kappler, C. Schmidt, Iron lung: How rice roots induce iron redox changes in the rhizosphere and create niches for microaerophilic Fe(II)-oxidizing bacteria. Environ. Sci. Technol. Lett. 6, 600-605 (2019).
- 12. J. Lee et al., Label-free multiphoton imaging of microbes in root, mineral, and soil matrices with time-gated coherent Raman and fluorescence lifetime imaging. Environ. Sci. Technol. 56, 1994-2008 (2022).
- 13. P. Cai et al., Soil biofilms: Microbial interactions, challenges, and advanced techniques for ex-situ characterization. Soil Ecol. Lett. 1, 85-93 (2019).
- L. Rochat, M. Péchy-Tarr, E. Baehler, M. Maurhofer, C. Keel, Combination of fluorescent reporters for simultaneous monitoring of root colonization and antifungal gene expression by a biocontrol pseudomonad on cereals with flow cytometry. Mol. Plant Microbe Interact. 23, 949-961 (2010).
- S. R. P. Pavani et al., Three-dimensional, single-molecule fluorescence imaging beyond the diffraction limit by using a double-helix point spread function. Proc. Natl. Acad. Sci. U.S.A. 106, 2995-2999 (2009).
- L. Von Diezmann, Y. Shechtman, W. E. Moerner, Three-dimensional localization of single molecules for super-resolution imaging and single-particle tracking. Chem. Rev. 117, 7244-7275
- 17. T. Wu, J. Lu, M. D. Lew, Dipole-spread-function engineering for simultaneously measuring the 3D orientations and 3D positions of fluorescent molecules. Optica 9, 505 (2022).
- P. Sarder, A. Nehorai, Deconvolution methods for 3-D fluorescence microscopy images. IEEE Signal Process. Mag. 23, 32-45 (2006).
- C. Roider, R. Heintzmann, R. Piestun, A. Jesacher, Deconvolution approach for 3D scanning microscopy with helical phase engineering. Opt. Express 24, 15456 (2016).
- K. Yanny et al., Miniscope3D: Optimized single-shot miniature 3D fluorescence microscopy. Light Sci. Appl. 9, 171 (2020).
- 21. L. Tian, L. Waller, Quantitative differential phase contrast imaging in an LED array microscope. Opt. Express 23, 11394 (2015).
- M. Chen, Z. F. Phillips, L. Waller, Quantitative differential phase contrast (DPC) microscopy with computational aberration correction. Opt. Express 26, 32888 (2018).
- U. Schnars, W. Jueptner, *Digital Holography* (Springer-Verlag, 2005).
 W. Osten *et al.*, Recent advances in digital holography [Invited]. *Appl. Opt.* **53**, G44 (2014).
- H. Zhou, M. M. R. Hussain, P. P. Banerjee, A review of the dual-wavelength technique for phase imaging and 3D topography. *Light: Adv. Manuf.* **3**, 17 (2022).
 G. Zheng, R. Horstmeyer, C. Yang, Wide-field, high-resolution Fourier ptychographic microscopy. 25.
- 26 Nat. Photon 7, 739-745 (2013).
- S. Dong \textit{et al.,} Aperture-scanning Fourier ptychography for 3D refocusing and super-resolution macroscopic imaging. Opt. Express 22, 13586 (2014).
- G. Zheng, C. Shen, S. Jiang, P. Song, C. Yang, Concept, implementations and applications of Fourier ptychography. Nat. Rev. Phys. 3, 207-223 (2021).
- Y. Park, G. Popescu, K. Badizadegan, R. R. Dasari, M. S. Feld, Diffraction phase and fluorescence microscopy. Opt. Express 14, 8263 (2006).
- N. Pavillon et al., Cell morphology and intracellular ionic homeostasis explored with a multimodal approach combining epifluorescence and digital holographic microscopy. J. Biophotonics 3, 432-436 (2010).
- 31. E. Shaffer, N. Pavillon, C. Depeursinge, Single-shot, simultaneous incoherent and holographic microscopy. J. Microscopy 245, 49-62 (2012).
- Y. Liu, J. Suo, Y. Zhang, Q. Dai, Single-pixel phase and fluorescence microscope. Opt. Express 26, 32451 (2018)
- S. Tayal, V. Singh, T. Kaur, N. Singh, D. S. Mehta, Simultaneous fluorescence and quantitative phase imaging of MG63 osteosarcoma cells to monitor morphological changes with time using partially spatially coherent light source. Methods Appl. Fluoresc. 8, 035004 (2020).

ACKNOWLEDGMENTS. We thank Dmitri Mavrodi for kindly providing wild-type P. synxantha 2-79 and P. synxantha 2-79 P_{tac}-mCherry. We also thank Nate Glasser at the Resnick Ecology and Biosphere Engineering Facility for the assistance in capturing confocal images. We are grateful to the Resnick Sustainability Institute for enabling resources and financial support. R.E.A. was further supported by an NSF Postdoctoral Research Fellowship in Biology (Grant No. 2209379).

Author affiliations: ^aDivision of Engineering and Applied Science, California Institute of Technology, Pasadena, CA 91125; ^bDivision of Biology and Biological Engineering, California Institute of Technology, Pasadena, CA 91125; and ^cDivision of Geological and Planetary Sciences, California Institute of Technology, Pasadena, CA 91125

- 34. S. K. Rajput et al., Multi-physical parameter cross-sectional imaging of quantitative phase and fluorescence by integrated multimodal microscopy. IEEE J. Select. Top. Quantum Electron. 27, 1-9 (2021).
- X. Quan et al., Multimodal microscopy: Fast acquisition of quantitative phase and fluorescence imaging in 3D space. *IEEE J. Select. Top. Quantum Electron.* 27, 1–11 (2021).
- S. Tayal et al., Design and development of integrated TIRF and common-path quantitative phase microscopic health care system with high stability. Opt. Lasers Eng. 155, 107057
- B. Marthy, M. Bénéfice, G. Baffou, Single-shot quantitative phase-fluorescence imaging using cross-grating wavefront microscopy. Sci. Rep. 14, 2142 (2024).
- C. Shen, M. Liang, A. Pan, C. Yang, Non-iterative complex wave-field reconstruction based on Kramers-Kronig relations. Photon. Res. 9, 1003 (2021).
- G. S. Settles, Schlieren and Shadowgraph Techniques (Springer Berlin Heidelberg, 2001).
- G. S. Settles, M. J. Hargather, A review of recent developments in schlieren and shadowgraph techniques. Meas. Sci. Technol. 28, 042001 (2017).
- S. Lowenthal, Y. Belvaux, Observation of phase objects by optically processed Hilbert transform. Appl. Phys. Lett. 11, 49-51 (1967).
- J. Ojeda-Castaneda, L. R. Berriel-Valdos, Classification scheme and properties of schlieren techniques. Appl. Opt. 18, 3338 (1979).
- J. Ojeda-Castaneda, E. Jara, Isotropic Hilbert transform by anisotropic spatial filtering. Appl. Opt. 25, 4035 (1986)
- S. Bernet, A. Jesacher, S. Fürhapter, C. Maurer, M. Ritsch-Marte, Quantitative imaging of complex samples by spiral phase contrast microscopy. Opt. Express 14, 3792 (2006).
- R. De, L. Kronig, On the theory of dispersion of X-rays. J. Opt. Soc. Am. 12, 547 (1926).
- Y. Baek, K. Lee, S. Shin, Y. Park, Kramers-Kronig holographic imaging for high-space-bandwidth product. Optica 6, 45 (2019).
- R. Claveau et al., Digital refocusing and extended depth of field reconstruction in Fourier ptychographic microscopy. Biomed. Opt. Express 11, 215 (2020).
- M. Liang et al., All-in-focus fine needle aspiration biopsy imaging based on Fourier ptychographic microscopy. J. Pathol. Inform. 13, 100119 (2022).
- 49. O. Zhang et al., Six-dimensional single-molecule imaging with isotropic resolution using a multiview reflector microscope. Nat. Photonics 17, 179-186 (2023).
- C. Guo, W. Liu, X. Hua, H. Li, S. Jia, Fourier light-field microscopy. *Opt. Express* **27**, 25573 (2019).
- 51. A. C. Kak, M. Slaney, Principles of Computerized Tomographic Imaging (Society for Industrial and Applied Mathematics, 2001).
- ${\sf N.\,Dey}\,\textit{et\,al.}, {\sf Richardson-Lucy}\,\textit{algorithm}\,\textit{with}\,\, {\sf total}\,\, {\sf variation}\,\, {\sf regularization}\,\, {\sf for}\,\, {\sf 3D}\,\, {\sf confocal}\,\, {\sf variation}\,\, {\sf varia$ microscope deconvolution. Microsc. Res. Tech. 69, 260-266 (2006).
- F. Dell'Acqua et al., A model-based deconvolution approach to solve fiber crossing in diffusionweighted MR imaging. IEEE Trans. Biomed. Eng. 54, 462-472 (2007).
- A. S. Backer, M. P. Backlund, M. D. Lew, W. E. Moerner, Single-molecule orientation measurements with a quadrated pupil. Optics Lett. 38, 1521 (2013).
- H. Zhou et al., Fourier ptychographic microscopy image stack reconstruction using implicit neural representations. Optica 10, 1679 (2023).
- C. Zuo, J. Sun, J. Li, A. Asundi, Q. Chen, Wide-field high-resolution 3D microscopy with Fourier ptychographic diffraction tomography. Opt. Lasers Eng. 128, 106003 (2020).
- M. Liang, C. Yang, Implementation of free-space Fourier Ptychography with near maximum system numerical aperture. Opt. Express 30, 20321 (2022).
- T. Colomb et al., Extended depth-of-focus by digital holographic microscopy. Opt. Lett. 35, 1840 (2010).
- W. O. Saxton, W. Baumeister, The correlation averaging of a regularly arranged bacterial cell envelope protein. *J. Microscopy* **127**, 127–138 (1982).
- 60. O. V. Mavrodi et al., Root exudates alter the expression of diverse metabolic, transport, regulatory, and stress response genes in rhizosphere pseudomonas. Front. Microbiol. 12, 651282 (2021).
- D. V. Mavrodi et al., Accumulation of the antibiotic phenazine-1-carboxylic acid in the rhizosphere of dryland cereals. Appl. Environ. Microbiol. 78, 804-812 (2012).
- R. M. Boiteau et al., Metabolic interactions between Brachypodium and Pseudomonas fluorescens under controlled iron-limited conditions. mSystems 6, e00580-20 (2021).
- N. A. Fujishige, N. N. Kapadia, A. M. Hirsch, A feeling for the micro-organism: Structure on a small scale. Biofilms on plant roots. Bot. J. Linn. Soc. 150, 79-88 (2006).
- J. H. Merritt, D. E. Kadouri, G. A. O'Toole, Growing and analyzing static biofilms. Curr. Protoc. Microbiol. 1, Unit-1B.1 (2005).
- E. K. Perry, D. K. Newman, Prevalence and correlates of phenazine resistance in culturable bacteria from a dryland wheat field. Appl. Environ. Microbiol. 88, e02320-21 (2022).
- Y. Park, C. Depeursinge, G. Popescu, Quantitative phase imaging in biomedicine. Nat. Photon 12, 578-589 (2018). S. Jiang et al., Ptychographic sensor for large-scale lensless microbial monitoring with high
- spatiotemporal resolution. Biosens. Bioelectron. 196, 113699 (2022). M.-A. Dollard, P. Billard, Whole-cell bacterial sensors for the monitoring of phosphate
- bioavailability. J. Microbiol. Methods 55, 221-229 (2003).

- 69. H. Sakhtah, A. M. Price-Whelan, L. Dietrich, Microbial Phenazines: Biosynthesis, Agriculture and Health (Springer, Berlin, Heidelberg, 2013), pp. 19-42, 10.7916/D81J98PJ.
- B. Mellbye, M. Schuster, Physiological framework for the regulation of quorum sensing-dependent public goods in Pseudomonas aeruginosa. *J. Bacteriol.* **196**, 1155–1164 (2014).

 D. L. McRose, D. K. Newman, Redox-active antibiotics enhance phosphorus bioavailability. *Science*

- 3/1, 1033–1037 (2021).

 V.Jensen et al., Alle expression in Pseudomonas aeruginosa is modulated by the Pseudomonas quinolone signal via PhoB-dependent and -independent pathways. J. Bacteriol. 188, 8601–8606 (2006).

 C. Molina-Santiago et al., A noninvasive method for time-lapse imaging of microbial interactions and colony dynamics. Microbiol. Spectr. 10, e0093922 (2022).

 P. Bravo, S. Lung Ng, K. A. MacGillivray, B. K. Hammer, P. J. Yunker, Vertical growth dynamics of biofilms. Proc. Natl. Acad. Sci. U.S.A. 120, e2214211120 (2023).

 A. J. Paula, G. Hwang, H. Koo, Dynamics of bacterial population growth in biofilms resemble spatial and structural aspects of urbanization. Nat. Commun. 11, 1354 (2020).
- 76. M. Futo et al., A novel time-lapse imaging method for studying developing bacterial biofilms. Sci. Rep. 12, 21120 (2022).
- L. Eigentler et al., Founder cell configuration drives competitive outcome within colony biofilms. ISME J. 16, 1512-1522 (2022).
- L. Eigentler, F. A. Davidson, N. R. Stanley-Wall, Mechanisms driving spatial distribution of residents in colony biofilms: An interdisciplinary perspective. *Open Biol.* 12, 220194 (2022).
 W. G. Sunda, N. M. Price, F. M. M. Morel, "Trace metal ion buffers and their use in culture studies" in
- Algal Culturing Techniques, R. A. Andersen, Ed. (Elsevier/Academic Press, 2005), pp. 35–63.
 K.-H. Choi, H. P. Schweizer, mini-Tn 7 insertion in bacteria with single att Tn 7 sites: Example
- Pseudomonas aeruginosa. *Nat. Protoc.* **1**, 153–161 (2006).
 D. G. Gibson *et al.*, Enzymatic assembly of DNA molecules up to several hundred kilobases. *Nat.*
- Methods **6**, 343–345 (2009).
- O. Zhang, Investigating 3D microbial community dynamics of the rhizosphere using quantitative phase and fluorescence microscopy [Data set]. OSF. https://osf.io/ak4wg/. Deposited 13 February 2024.